Confirmation of SRGt 062340.2-265751 as a nova-like cataclysmic variable with a possible magnetic nature

V. A. Cúneo⋆[1], A. D. Schwope[1], J. Kurpas[1], A. Avakyan[2], J. Brink[1,3], D. A. H. Buckley[4,5,6], C. Maitra[7], and M. Veresvarska[8]

[1] Leibniz-Institut für Astrophysik Potsdam (AIP), An der Sternwarte 16, 14482 Potsdam, Germany
[2] Institut für Astronomie und Astrophysik Tübingen, Universität Tübingen, Sand 1, Tübingen, 72076, Baden-Württemberg, Germany
[3] Potsdam University, Institute for Physics and Astronomy, Karl-Liebknecht-Straße 24/25, 14476 Potsdam, Germany
[4] South African Astronomical Observatory, PO Box 9, Observatory Road, Observatory 7935, Cape Town, South Africa
[5] Department of Astronomy, University of Cape Town, Private Bag X3, Rondebosch 7701, South Africa
[6] Department of Physics, University of the Free State, PO Box 339, Bloemfontein 9300, South Africa
[7] Max-Planck-Institut für Extraterrestrische Physik, Gießenbachstraße 1, 85748 Garching, Germany
[8] Department of Physics, Centre for Extragalactic Astronomy, Durham University, South Road, Durham DH1 3LE, UK

Received 27 August 2025 / Accepted 4 November 2025

ABSTRACT

SRGt 062340.2-265751, a cataclysmic variable identified by *SRG*/eROSITA thanks to its significant X-ray variability, remains poorly characterised despite the multi-wavelength follow-up. We present spectral and timing analyses from the first dedicated X-ray and ultraviolet observations with *XMM-Newton*, complemented by *SRG*/eROSITA data from four all-sky surveys (eRASS1-4) and ASAS-SN optical photometry. Our timing analysis reveals a $>8\sigma$ significant modulation at 3.6 ± 0.5 hours, likely representing the orbital period. Long-term ASAS-SN monitoring confirms the source as a VY Sculptoris-type nova-like system, while short-timescale X-ray and ultraviolet variability, down to a few minutes, suggests a possible underlying magnetic white dwarf. Two additional significant X-ray modulations at 43 ± 1 min and 36.0 ± 0.7 min tentatively point to the spin period of an intermediate polar. The best-fit *XMM-Newton* energy spectra reveal a multi-temperature thermal plasma (kT = 0.23, 0.94, and 5.2 keV), while the *SRG*/eROSITA spectra are consistent with a single-temperature thermal plasma of a few keV. We estimate unabsorbed X-ray luminosities of $\gtrsim 10^{32}$ erg s^{-1} (0.2−12 keV). Broadband spectral energy distribution modelling, from near-ultraviolet to infrared, indicates a disc-dominated system consistent with a nova-like classification. We discuss these results in the context of the source's confirmed nova-like classification and its possible magnetic nature, a scenario increasingly supported by discoveries of intermediate polars exhibiting VY Sculptoris-type nova-like features.

Key words. (Stars:) novae, cataclysmic variables – X-rays: stars – stars: individual: SRGt 062340.2-265751

. Introduction

ataclysmic variables (CVs), the most common type of accreting white dwarfs, are close binaries in which a white dwarf accretes matter from a low-mass companion star that fills its Roche obe (see Warner 2003, for a review). Depending on the strength f the white dwarf's magnetic field, these systems are typically lassified as either magnetic (B > 1 MG) or non-magnetic. Magetic systems comprise polars and intermediate polars (IPs). In olars, the magnetic field is so strong (B ≥ 10 MG) that it preents the formation of an accretion disc. Instead, matter is chanelled along magnetic field lines and impacts the white dwarf near its magnetic poles, forming a shock-heated region that emits X-rays (for a review, see Cropper 1990). In these systems, the white dwarf's spin period ($P_{\rm spin}$) is typically synchronised with the orbital period ($P_{\rm orb}$; see, for example, Schwope 2025). IPs, by contrast, have weaker magnetic fields, allowing the formation of a truncated accretion disc. Therefore, matter is first accreted through the disc before being redirected along magnetic field lines to the poles, where it shocks and heats up similarly to polars. The post-shock plasma then cools via bremsstrahlung radiation, producing hard X-rays (see the review by Patterson 1994). Since the magnetic and rotational axes are usually misaligned, the X-ray emission is modulated at $P_{\rm spin}$. In these systems, $P_{\rm spin}$ and $P_{\rm orb}$ are not synchronised, and both modulations are typically identified through timing analysis, serving as a key diagnostic of their IP nature (e.g. Mukai 2017). In contrast, non-magnetic systems, which are mainly divided into dwarf novae and nova-likes, accrete matter through an accretion disc. Dwarf novae, the class from which the term cataclysmic variables originates, are transient systems that undergo outbursts when the disc becomes thermally unstable after accumulating enough matter (see reviews by Osaki 1996; Hameury 2020). Nova-likes, on the other hand, accrete matter persistently at high rates ($\dot{M} \sim 10^{-8} M_\odot\ yr^{-1}$, Puebla et al. 2007; Ballouz & Sion 2009) through a hot stable disc. In particular, a subclass of nova-likes known as VY Sculptoris (VY Scl) exhibit long-term variability in their optical light curves, including sporadic low states characterised by brightness drops of ≳1 mag (e.g. King & Cannizzo 1998).

The *Spektrum-Roentgen-Gamma* (*SRG*) mission (Sunyaev et al. 2021) conducted 4.4 all-sky surveys between December 2019 and February 2022 using its two onboard instruments: the Mikhail Pavlinsky ART-XC (Pavlinsky et al. 2021) and the extended ROentgen Survey with an Imaging Telescope Array

⋆ Corresponding author: virginiacuneo@gmail.com

Table 1. X-ray observing log.

Observatory	SKYTILE / ID	Epoch	Date (yyyy-mm-dd)	MJD	Exposure [s]	Instrument	Mode	Filter	Net exposure [s]	Rate [cts s^{-1}]
SRG	095108	eRASS1	2020-04-07	58946.9	247	eROSITA	Survey	FILTER	107	0.74 ± 0.06
	095108	eRASS2	2020-10-11	59133.4	236	eROSITA	Survey	FILTER	102	2.8 ± 0.1
	095108	eRASS3	2021-04-05	59310.1	323	eROSITA	Survey	FILTER	141	2.53 ± 0.09
	095108	eRASS4	2021-10-07	59494.6	356	eROSITA	Survey	FILTER	154	1.40 ± 0.06
XMM-Newton	0901220101		2023-04-21	60055.5	46000	EPIC-pn	Small Window	THIN1	44139	1.075 ± 0.006
						EPIC-MOS1	Small Window	THIN1	44626	0.236 ± 0.002
						EPIC-MOS2	Small Window	THIN1	44606	0.284 ± 0.003
						RGS1	Spec. HER+SES		44830	0.049 ± 0.001
						RGS2	Spec. HER+SES		44910	0.051 ± 0.001
						OM	Fast	UVM2	41398	81.13 ± 0.04

(eROSITA, Predehl et al. 2021). Following the release of the first eROSITA all-sky survey (eRASS1), the number of known X-ray sources reported in the literature increased by more than 60% (Merloni et al. 2024). In particular, eROSITA has facilitated the discovery of new CV candidates that were subsequently confirmed through follow-up multi-wavelength observations, especially optical spectroscopy (Schwope et al. 2022b; Ok et al. 2023).

SRGt 062340.2-265751 (hereafter SRGt 062340) was identified during the second eROSITA all-sky survey (eRASS2), which revealed a factor-of-two increase in X-ray flux compared to eRASS1 (Schwope et al. 2020a). Its optical counterpart, with $G = 12.4$ mag and a distance of 496 ± 4 pc, was identified in Gaia DR3 (Gaia DR3 2899766827964264192; Schwope et al. 2022a). Notably, this counterpart had already been reported in 2017 by Denis Denisenko and designated DDE 79 in the International Variable Star Index (VSX) catalogue[1] of the American Association of Variable Star Observers (AAVSO) and by the Zwicky Transient Facility (ZTF19aaabzuh). Optical spectroscopy of the Gaia counterpart, obtained using the Wide Field Spectrograph (WiFeS) on the 2.3 m telescope at the Australian National University (ANU) and the High Resolution Spectrograph (HRS) on the 10 m Southern African Large Telescope (SALT), unequivocally identified the source as a CV. The SALT/HRS spectrum revealed the presence of the Bowen blend at $\sim\lambda4640$, a feature commonly observed in magnetic CVs (e.g. Schachter et al. 1991). Archival serendipitous X-ray observations of the SRGt 062340 field, including *ROSAT* (1RXS J062339.8-265744), *XMM-Newton*, and *Swift*/XRT (2SXPS J062339.9-265751), revealed a high degree of X-ray variability (Schwope et al. 2022a), consistent with the eROSITA findings and suggestive of an IP (e.g. Norton et al. 1996). However, this system's most puzzling property is its optical photometric variability. The Transiting Exoplanet Survey Satellite (TESS; Ricker et al. 2015) observed the source from 15 December 2018 to 6 January 2019, and again from 18 December 2020 to 13 January 2021. During the first epoch, a clear modulation at 3.9 h was detected (Pichardo-Marcano 2020), yet this periodicity was absent in the second epoch (Schwope et al. 2022a), which instead revealed a ~25 min modulation. A period search in archival photometry from the All-Sky Automated Survey for Supernovae (ASAS-SN; Shappee et al. 2014; Hart et al. 2023), confirmed the 3.9 h periodicity detected during the first TESS observation. Additionally, high-speed photometry obtained with the Sutherland High Speed Optical Camera (SHOC; Coppejans et al. 2013) on the 1 m telescope at the South African Astronomical Observatory (SAAO) revealed modulations at ~35 min. The source is clearly variable, with potential periodicities at different wavelengths. However, despite the extensive datasets analysed, no periodic signal could be consistently confirmed across all observations. Given its unusual properties, Schwope et al. (2022a) suggested that SRGt 062340 could be an X-ray underluminous IP, an overluminous non-magnetic CV, or perhaps a new type of CV.

To investigate the nature of the source and search for potential periodic modulations, we obtained a dedicated *XMM-Newton* observation of SRGt 062340, lasting 46 ks, in April 2023. In the following sections, we present an analysis of these new follow-up observations, along with the complete eROSITA dataset and archival broadband photometry from the near-UV to the IR. A companion paper by Brink et al. (in prep.) will present a detailed analysis of extensive optical photometry and spectroscopy.

2. Observations

2.1. XMM-Newton

We observed SRGt 062340 with the *XMM-Newton Observatory* (Jansen et al. 2001) on 21 April 2023 for a total exposure of 46 ks, using all onboard instruments (see Table 1 for the observing log). Calibrated events lists and scientific data products were extracted using the Science Analysis System (SAS, v21.0.0) in combination with HEASOFT v6.33.1 and the latest calibration files, following standard data reduction procedures.[2]

We processed the data collected by the pn detector (Strüder et al. 2001) and the Metal Oxide Semi-conductor (MOS1 and MOS2; Turner et al. 2001) detectors of the European Photon Imaging Camera (EPIC), using the SAS tasks `epproc` and `emproc`, respectively. Source events were extracted using a circular region with a radius of 30″ in all detectors. Background events were selected from two rectangular regions within the EPIC-pn window, carefully avoiding the readout direction, and from two circular regions with a radius of 50″ in CCDs adjacent to the source CCD in the EPIC-MOS data. We filtered the event files to exclude periods of background flaring using a sigma-clipping algorithm with a 3σ threshold, and used `tabgtigen` to define the corresponding good time intervals. We note, however, that the observation was barely affected by flaring, with only 500 s and 1000 s removed from the EPIC-pn and EPIC-MOS2 datasets, respectively, while no filtering was required for EPIC-MOS1. Additional cleaning was applied using the recommended filters: `FLAG = 0` and `PATTERN` $\leq$ 4 for EPIC-pn, and `FLAG = 0` and `PATTERN` $\leq$ 12 for EPIC-MOS. A barycentric correction was then applied to the final event lists using

[1] https://vsx.aavso.org/index.php?view=detail.top&oid=477558

[2] https://www.cosmos.esa.int/web/xmm-newton/sas-threads

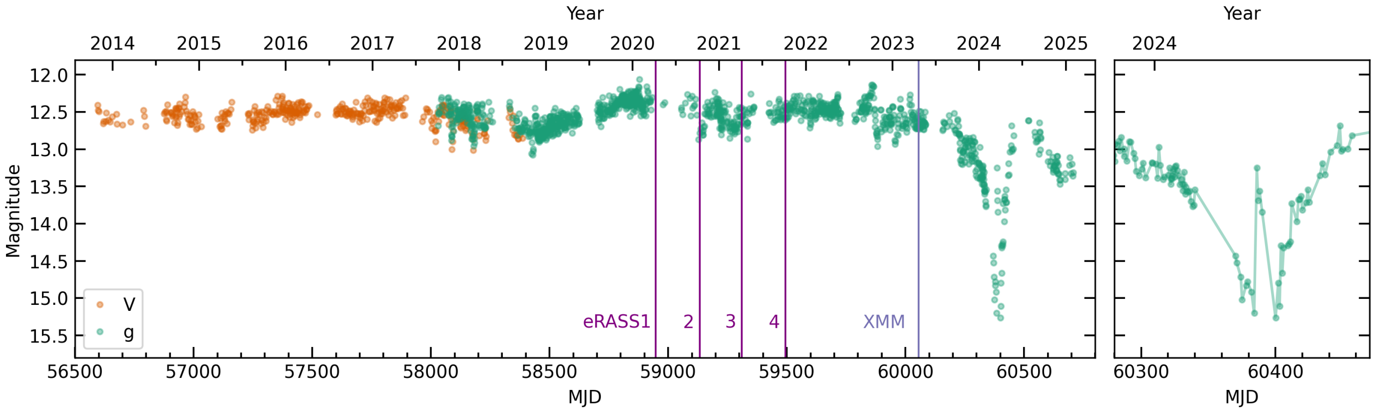

Fig. 1. *Left panel:* Long-term ASAS-SN light curve of SRGt 062340, combining V- and g-band magnitudes. The purple vertical lines indicate the epochs of the eROSITA observations, while the lilac line marks the epoch of the *XMM-Newton* observation. *Right panel:* Detailed view of the light curve between MJD 60280 and MJD 60470.

the `barycen` task with DE200 ephemeris. Background-corrected light curves were produced using `evselect` and `epiclccorr`. Following standard procedures, we also generated source and background spectra, as well as response matrix files (RMFs) and ancillary response files (ARFs). The spectra were rebinned using `specgroup` to ensure a minimum of 25 counts per spectral bin, to avoid oversampling the full width at half-maximum of the energy resolution by more than a factor of three, and to link all the spectral files consistently.

We used the SAS task `rgsproc` to process the data from the Reflection Grating Spectrometers (RGS1 and RGS2; den Herder et al. 2001) and obtain the data products. The sigma-clipping algorithm was applied again to check for flaring events on CCD 9, which is the closest to the telescope's optical axis and the most sensitive to background flares. However, no enhanced activity was detected. When analysing RGS data, it is important to note that one CCD chip in each detector failed early in the mission due to electronic issues, affecting the spectral ranges 11−14 Å (∼0.9−1.1 keV) in RGS1 and 20−24 Å (∼0.5−0.6 keV) in RGS2. Finally, we used `rgscombine` to merge the RGS1 and RGS2 spectra and `specgroup` to rebin the spectra to a minimum of 25 counts per bin, set an oversampling factor of 3, and link the spectral files.

The Optical Monitor (OM; Mason et al. 2001) was operated in fast mode using the UVM2 filter ($\lambda_{\rm eff}$ = 2310 Å). We generated a light curve using the `omfchain` task, and then applied the barycentric correction using the `barycen` task with DE200 ephemeris.

2.2. SRG/eROSITA

The field of SRGt 062340 was observed during four all-sky scans (eRASS1-4) using the eROSITA instrument aboard the *SRG* mission, as part of the eROSITA All-sky Survey (Merloni et al. 2024). These observations, with a total exposure of ∼1.1 ks, span approximately 1.5 years (from April 2020 to October 2021; see the observing log in Table 1) and allow us to probe the long-term evolution of SRGt 062340 in the 0.2−8 keV X-ray band. In accordance with the eROSITA scanning pattern, each all-sky scan consists of seven to nine slews over the field, separated by four hours (one eroday), which is the time required for the instrument to complete one full rotation (Merloni et al. 2024).

We obtained event lists containing detected X-ray photons from all seven X-ray telescopes in eROSITA, which were processed with the latest pipeline (version c030). These were cleaned using the eROSITA Science Analysis Software System (eSASS; user version 240410.0.4, Brunner et al. 2022), retaining only photons with valid patterns (`PATTERN` ≤ `15`) and standard good quality flagging criteria (`FLAG` = 0xE000F000; e.g. see section 3.2.2 in Kurpas et al. 2024, for more details). We also removed high-background flaring periods by applying the `flaregti` task to create updated good time interval (GTI) lists, which were then applied to the event lists. To identify SRGt 062340 and nearby field sources, we conducted a source detection within 20′ of SRGt 062340's position in the 0.2−2.3 keV band, following the methods of Brunner et al. (2022) and Merloni et al. (2024). Based on these results, we applied the `srctool` task to define optimised source and background regions, extract source spectra, and generate light curves. The spectra were binned to contain a minimum of 1 and 25 counts per spectral bin using the `grppha` task. The light curve was binned into 1 eroday intervals (see above for definition), ensuring one data point per slew containing photons from SRGt 062340.

3. Analysis and results

3.1. Long-term optical variability

To analyse the optical evolution of SRGt 062340, we extracted a long-term ASAS-SN light curve using the ASAS-SN Sky Patrol V2.0.[3] The resulting optical light curve, shown in the left panel of Fig. 1, exhibits significant variability. Between November 2013 (MJD ∼ 56600) and June 2023 (MJD ∼ 60100) the V/g-band magnitudes oscillated between ∼13 and 12 mag. Our eROSITA and *XMM-Newton* observations were conducted during this period and are indicated in Fig. 1. The most dramatic variability, however, occurred from September 2023 (MJD ∼ 60200), when the source exhibited two drops in brightness. The first was a sharp ∼3 mag decline to $g \simeq 15.2$, interrupted by a brief rebrightening around MJD ∼ 60390 (duration < 20 days) that reached $g \simeq 13.5$ (see the right panel of Fig. 1), after which the source settled again near $g \simeq 15.3$. It then recovered to approximately its pre-dip level ($g \simeq 12.6$) before a second ∼1 mag decline to $g \simeq 13.5$. Such low states are characteristic of the VY Scl subclass of nova-likes (King & Cannizzo 1998; Warner 2003), firmly establishing SRGt 062340 as a member

[3] http://asas-sn.ifa.hawaii.edu/skypatrol/

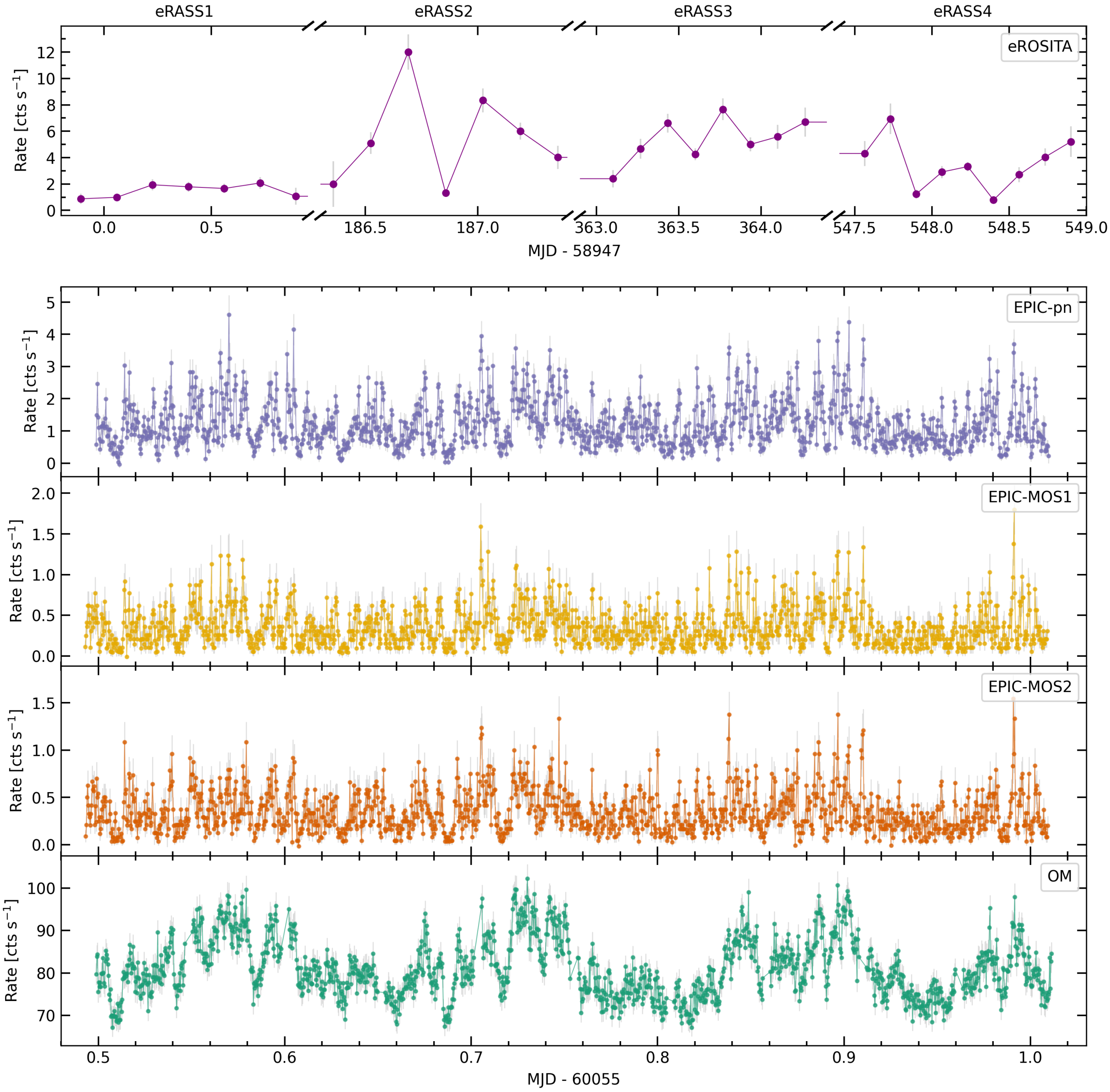

Fig. 2. *Top panel:* eROSITA light curve of SRGt 062340 in the 0.2−8 keV energy band across the four all-sky surveys (eRASS1-4). Each data point represents the mean rate of a single scan over the source position, separated by an eroday (4 h; see text for more details). *Second to fifth panels: XMM-Newton*/EPIC-pn, EPIC-MOS1, and EPIC-MOS2 30 s binned light curves of SRGt 062340 in the 0.2−12 keV energy band, followed by the OM 30 s binned light curve obtained with the UVM2 filter.

of this group. The rebrightening during the first drop resembles the dwarf-nova-type outbursts reported during the low states of a few VY Scl systems (e.g. Pavlenko & Shugarov 1999); however, such rebrightenings are rare (e.g. Hameury 2020).

3.2. X-ray and ultraviolet timing analysis

The top panel of Fig. 2 shows the eROSITA light curve of SRGt 062340 in the 0.2−8 keV energy band across the four all-sky surveys (eRASS1-4). In addition to the pronounced variability between eRASS1 and eRASS2, which led to the detection of the source, significant variability is evident throughout the dataset, both on long timescales (from one survey to the next, over ∼6 months) and on short timescales (from one scan of the source position to the next, over ∼4 h). To quantify the overall variability, we computed the maximum observed rate deviation, following Kurpas et al. (2024, see also Traulsen et al. 2020):

$$\mathrm{RATE\_VAR} = \max_{k,l\in[1,n]} \frac{|R_k - R_l|}{\sqrt{\sigma_k^2 + \sigma_l^2}}. \qquad (1)$$

Here R_k and R_l are the count rates at epochs k and l, and σ_k and σ_l are their corresponding uncertainties. The most significant variability (exceeding 8σ and corresponding to a rate change of more than 90%) occurs between MJD 59133.69 (eRASS2) and MJD 59495.40 (eRASS4).

In the second to fourth panels of Fig. 2, we present 30 s binned light curves extracted from the EPIC-pn, EPIC-MOS1,

Table 2. Summary of the peak values of the >5σ significant modulations detected in the Lomb-Scargle power spectra shown in Fig. 3.

	LS frequency [$\times10^{-4}$ Hz]	Gauss fit [$\times10^{-4}$ Hz]	Gauss fit [Time]	EPIC-pn sig.	OM sig.
EPIC-pn	0.760	0.8 ± 0.1	3.6 ± 0.5 h	8σ	>8σ
	3.911	3.9 ± 0.1	43 ± 1 min	5σ	1σ
	4.636	4.63 ± 0.09	36.0 ± 0.7 min	8σ	3σ
	7.856	7.9 ± 0.1	21.2 ± 0.3 min	6σ	3σ
	9.761	9.76 ± 0.09	17.1 ± 0.2 min	5σ	–
OM	0.759	0.8 ± 0.1	3.6 ± 0.5 h	8σ	>8σ
	1.371	1.37 ± 0.08	2.0 ± 0.1 h	<1σ	8σ
	1.905	1.9 ± 0.1	1.4 ± 0.1 h	2σ	5σ
	6.030	6.02 ± 0.09	27.7 ± 0.4 min	<1σ	5σ

and EPIC-MOS2 photon event lists in the 0.2−12 keV energy range. The bin size was chosen to avoid empty bins while maintaining high cadence. In the bottom panel of Fig. 2, we also show the ultraviolet (UV) OM 30 s binned light curve. Clear variability is observed in all the *XMM-Newton* light curves, with notable similarities between the different datasets.

Since EPIC-pn and OM produced the highest count rates, we focused our timing analysis on these instruments to search for periodic modulations. We used the Lomb-Scargle algorithm (Lomb 1976; Scargle 1982) to search for periodic modulations within the range 60 − 22000 s, defined by twice the bin size (corresponding to the Nyquist frequency) and approximately half of the duration of the observation (corresponding to the longest detectable modulation). Fig. 3 shows the resulting power spectra, revealing significant power peaks at several frequencies. We marked the peak values of the >5σ significant modulations in Fig. 3 and listed them in Table 2. All significance levels indicate the probability that the observed power is not due to white noise, with the likelihood of peaks arising from white noise estimated through the false-alarm probability (Baluev 2008). The errors correspond to half the full width at half-maximum of a Gaussian fit to each peak. Table 2 also includes the significance levels of the modulations in the other power spectrum (EPIC-pn for OM, and vice versa). The only modulation detected with high significance by both EPIC-pn and OM is the highest peak in the power spectra at ∼ 7.6×10^{-5} Hz (3.6±0.5 h), which we tentatively interpret as the orbital period (see Section 4.1 for further discussion). We analysed possible correlations between the significant modulations to establish their origin. We found that if P_{orb} = 3.6 h, the modulations at 2 and 1.4 h are likely the first and second harmonics, respectively, within uncertainties on all values. Additionally, we identified two potential candidates for a spin period that provide meaningful relations to the other significant modulations: 36 min, the second strongest peak in the EPIC-pn power spectrum and nearly as significant as the 3.6 h peak, and 43 min. We note, however, that these interpretations should be treated with caution until further evidence clarifies their nature. Table 3 summarises the correlations between the modulations listed in Table 2 for these two hypothetical cases. Fig. A.1 presents the EPIC-pn and OM light curves folded on the 3.6 h, 43 min, and 36 min modulations. The 43 min signal shows no clear modulation in either dataset, yet its pulse fraction is comparable to that of the more evident 36 min modulation: 24% for EPIC-pn and 2.4 − 2.8% for OM. In both cases, the OM folded light curve exhibits very low pulse fractions, reflecting the weak presence of these signals at ultraviolet wavelengths.

We also computed the power spectra of the EPIC-pn data across multiple energy bands (0.2–0.5, 0.5–1, 0.5–3, 1–3, and 3–12 keV). However, these were less significant than those de-

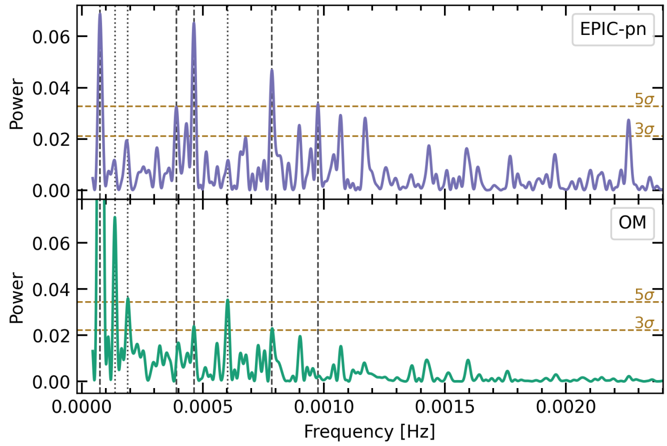

Fig. 3. Lomb-Scargle power spectra of the EPIC-pn light curve in the 0.2−12 keV energy band (top) and the OM light curve obtained with the UVM2 filter (bottom). The dashed horizontal lines indicate the 3σ and 5σ power significance levels. The grey vertical lines (dashed for EPIC-pn and dotted for OM) denote the frequency of the peaks with a significance higher than 5σ. The frequencies and significance levels of the marked peaks are summarised in Table 2.

Table 3. Summary of the correlations between the modulations listed in Table 2, assuming $P_{orb} = \Omega^{-1}$ = 3.6 h and two possible $P_{spin} = \omega^{-1}$.

	Frequency	Period
If P_{spin} = 36 min	$\omega - \Omega$	43 min
	$2(\omega - \Omega)$	21.2 min
If P_{spin} = 43 min	$\omega - \Omega$	53.7 min[(*)]
	$\omega + \Omega$	36 min
	$2(\omega - \Omega)$	27.7 min
	2ω	21.2 min

Notes. [(*)] Although not listed in Table 2, this period corresponds to a peak in the EPIC-pn power spectrum with a significance below 3σ.

rived from the full energy band and did not provide any additional information. Nevertheless, the modulation we associate with $P_{\rm orb}$ was the only one consistently significant (> 3σ) across all analysed bands. We further examined the power spectra of the full-band (0.2–12 keV) EPIC-pn and OM observations by splitting each into two halves. Although the 3.6 h modulation could no longer be detected due to the reduced time interval, the shorter periodicities detected in the full observations were present in the first half but fell below 3σ significance in the second half for both EPIC-pn and OM. This transient behaviour is consistent with the variability previously reported for this source (e.g. in TESS datasets; Schwope et al. 2022a).

In addition to the periodic modulations discussed above, the *XMM-Newton* light curves (Fig. 2) show clear short-term variability. To quantify this, we again applied Eq. 1, measuring the maximum rate deviation over 5 min intervals. For the EPIC-pn light curve, the median significance across all 5 min intervals is 3.8σ, with individual intervals reaching ∼ 6σ and count rate changes of ∼ 90% on timescales of only a few minutes. To assess whether such flickering could be attributed solely to absorption, we simulated spectra with varying Galactic column densities ($N_{\rm H}$). Adopting an absorbed thermal plasma model (`tbabs*apec`) with kT = 8 keV, we found that $N_{\rm H}$ would need to increase by roughly three orders of magnitude to produce a

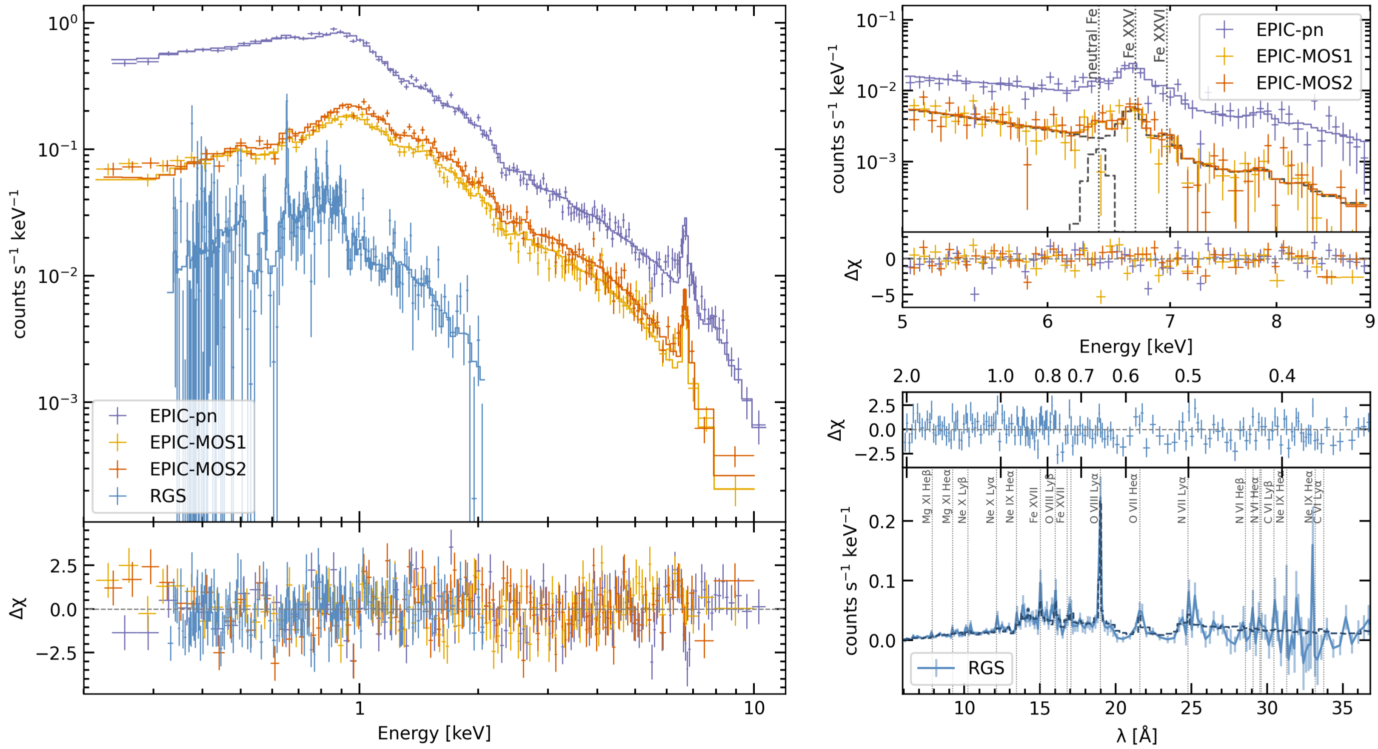

Fig. 4. *Left panel: XMM-Newton* energy spectra of SRGt 062340, shown with the best-fitting model (`TBabs*(apec+apec+apec)`). The bottom panel shows the normalised residuals. The best-fit parameters are listed in Table 4. *Top right panel:* Zoomed-in image of the Fe K complex, fitted with a `TBabs*(apec+gaussian)` model. The dashed lines represent the model components for the EPIC-MOS1 spectrum, shown as an example. The vertical dotted lines mark the expected energies of the different Fe-line components. *Bottom right panel:* RGS spectrum and best-fitting model, identical to those shown in the left panel, but plotted as a function of wavelength. The vertical lines indicate several prominent and commonly observed transitions.

90% drop in count rate. We therefore conclude that the flickering is primarily due to intrinsic variability in the source emission, rather than absorption effects. Applying the same methodology to the OM light curve over 5 min intervals yields a lower median variability significance of 2.4σ.

3.3. X-ray spectral analysis

The left panel of Fig. 4 shows the *XMM-Newton* spectra from the EPIC-pn, EPIC-MOS1, EPIC-MOS2, and RGS detectors. The EPIC spectra clearly exhibit the Fe K complex at 6–7 keV (see the top right panel of Fig. 4 for details), while the RGS spectrum reveals several emission lines at low energies (see the bottom right panel of Fig. 4 and the text below for details). We analysed all spectra using XSPEC (v.12.14.0b; Arnaud 1996), modelling interstellar absorption with the Tuebingen-Boulder model (`TBabs`) and adopting solar abundances from Wilms et al. (2000). A simultaneous fit was performed for all four spectra, linking model parameters across instruments and using χ^2 statistics. To account for calibration uncertainties, we included the `constant` scaling factor, left free to vary between instruments. A single `apec` model, representing a collisionally ionised plasma in thermal equilibrium, failed to adequately reproduce the data ($\chi^2_\nu(\nu)$ = 4.6(536)). Adding second and third `apec` components significantly improved the fit, suggesting emission from a cooling, multi-temperature plasma. Attempts to use multi-temperature isobaric cooling-flow models (`cevmkl` and `mkcflow`) or a partial covering absorber (`pcfabs`; see Norton & Watson 1989), often used in IPs to model X-ray absorption in the accretion column, did not improve the fit. We therefore adopted an absorbed three-component thermal plasma model (`TBabs*(apec+apec+apec)`) as the best fit. This model is shown in the left panel of Fig. 4, and the best-fitting parameters with 1σ uncertainties are listed in Table 4. We derived a Galactic column density of $N_{\rm H} = 3.4^{+0.3}_{-0.2} \times 10^{20}$ cm^{-2}, slightly lower than the value of 4.08×10^{20} cm^{-2} used by Schwope et al. (2022a). Using the `cflux` convolution model, we obtained an unabsorbed flux of 3.13×10^{-12} erg cm^{-2} s^{-1} in the 0.2–12 keV band, corresponding to a luminosity of 9.2×10^{31} erg s^{-1}, assuming a distance of 496 ± 4 pc (Schwope et al. 2022a).

A closer inspection of the Fe Kα complex (top right panel of Fig. 4) reveals, in addition to the expected Fe XXVI (H-like) line at 6.97 keV and Fe XXV (He-like) line at 6.7 keV, an emission excess corresponding to the neutral fluorescent Fe Kα line at 6.4 keV. While the Fe XXVI and Fe XXV lines are typical of emission from hot, ionised plasma, the 6.4 keV line likely indicates reflection off the surface of the white dwarf (e.g. Hellier & Mukai 2004; Rana et al. 2006), and possibly also off the accretion disc (Done & Osborne 1997; Ishida et al. 2009). The spectra shown in the top right panel of Fig. 4 were grouped to a minimum of 1 count per bin and analysed using the c-statistic. We initially fitted the 5–9 keV energy range with an absorbed thermal plasma plus a Gaussian component fixed at 6.4 keV to model the fluorescent line (`TBabs*(apec+gaussian)`). The Galactic column density was fixed to the value obtained from the simultaneous fit to *XMM-Newton* spectra ($N_{\rm H} = 3.4 \times 10^{20}$ cm^{-2}). As the Gaussian line width was poorly constrained, we next fitted only the thermal plasma component (`TBabs*apec`) excluding the 6.2–6.45 keV interval to account only for the ionised components. This gave a

Table 4. Best-fitting parameters for the four eROSITA epochs using the `TBabs*apec` model, and from the simultaneous fit to all *XMM-Newton* spectra using the `TBabs*(apec+apec+apec)` model.

Parameter		eRASS1	eRASS2	eRASS3	eRASS4	*XMM-Newton*
N_H	$[10^{20}\ \mathrm{cm}^{-2}]$	3.4 (fixed)	3.4 (fixed)	3.4 (fixed)	3.4 (fixed)	$3.4^{+0.3}_{-0.2}$
kT_1	[keV]	$2.3^{+2.1}_{-0.5}$	13^{+29}_{-5}	9^{+14}_{-3}	$4.8^{+1.3}_{-0.9}$	0.23 ± 0.01
kT_2	[keV]	–	–	–	–	$0.94^{+0.01}_{-0.02}$
kT_3	[keV]	–	–	–	–	5.2 ± 0.1
$\chi^2_\nu(\nu)^{(a)}$		117.51(127)	0.88(22)	0.94(26)	0.83(16)	1.35(532)
Flux $_{0.2-12\ \mathrm{keV}}{}^{(b)}$	$[10^{-12}\ \mathrm{erg\ cm^{-2}\ s^{-1}}]$	2.0 ± 0.2	17.4 ± 0.7	13.8 ± 0.5	6.1 ± 0.3	3.13 ± 0.01
Luminosity $_{0.2-12\ \mathrm{keV}}{}^{(c)}$	$[10^{32}\ \mathrm{erg\ s^{-1}}]$	0.59 ± 0.05	5.1 ± 0.2	4.1 ± 0.2	1.79 ± 0.09	0.92 ± 0.02
Luminosity $_{0.25-10\ \mathrm{keV}}{}^{(c)}$	$[10^{32}\ \mathrm{erg\ s^{-1}}]$	0.57 ± 0.05	4.7 ± 0.2	3.8 ± 0.2	1.71 ± 0.09	0.88 ± 0.01
Luminosity $_{0.01-100\ \mathrm{keV}}{}^{(c)}$	$[10^{32}\ \mathrm{erg\ s^{-1}}]$	0.63 ± 0.06	5.3 ± 0.2	4.2 ± 0.2	1.9 ± 0.1	1.05 ± 0.02

Notes. Uncertainties are given at the 1σ confidence levels. $^{(a)}$ For eRASS1, the value corresponds to the C-statistic (d.o.f). $^{(b)}$ Unabsorbed fluxes. $^{(c)}$ Unabsorbed luminosities were estimated assuming a distance of 496 ± 4 pc.

plasma temperature of $kT = 6.5 \pm 0.5$ keV. We then refitted the full 5−9 keV range, again including the Gaussian, this time fixing the plasma temperature at 6.5 keV. This fit yielded a Gaussian line width of $\sigma = 0.15 \pm 0.06$ keV, consistent with the EPIC energy resolution (of 150 eV at 6.4 keV). We therefore repeated the fit with the Gaussian width fixed at zero while allowing the plasma temperature to vary, obtaining $kT = 6.6 \pm 0.5$ keV, consistent with the previous value and indicative of a plasma hotter than the 5.2 keV derived from the full 0.2−12 keV fit. From this fit we derived an equivalent width (EW) for the 6.4 keV line of 150^{+60}_{-50} eV.[4]

The bottom right panel of Fig. 4 shows the RGS spectrum in wavelength units for clarity, along with the best-fitting model (`TBabs*(apec+apec+apec)`) from the simultaneous fit to the *XMM-Newton* spectra (see left panel of Fig. 4 and Table 4). Several prominent emission lines are visible, primarily from oxygen and iron, and possibly also from nitrogen, neon, carbon, and magnesium. The strongest oxygen features (H-like O VIII at 18.97 Å (0.65 keV) and the He-like O VII triplet at ∼21.6, 21.8, 22.1 Å (∼0.574, 0.568, 0.561 keV)) are well reproduced by our multi-temperature collisionally ionised plasma model. In contrast, several other features (e.g. C VI, N VI, and Ne IX) are not accounted for by the model and may instead originate from photoionisation (Mukai et al. 2003; Girish et al. 2007), which can occur in low-density environments or under sufficiently strong radiation fields; for SRGt 062340, an intense extreme-UV radiation field is the likely cause. However, even the well-modelled oxygen lines are insufficiently constrained (e.g. the individual components of the O VII triplet are blended) to permit reliable diagnostics from line ratios, such as temperature or density estimates.

To analyse the energy spectra from the four eROSITA observing epochs, we used spectra grouped to 25 counts per bin for eRASS2-4 and applied χ^2 statistics, while for eRASS1 we used a 1 count per bin spectrum (due to its lower number of counts) and applied the C-statistic. In all cases, the spectra were well described by a single absorbed thermal plasma model (`TBabs*apec`), with no significant residuals. We fixed the Galactic column density to the value obtained from the *XMM-Newton* spectral analysis (3.4×10^{20} cm^{-2}) and derived 1σ uncertainties for all fit parameters. The resulting spectra and best-fitting models are shown in Fig. 5, and the corresponding parameters are listed in Table 4. The derived plasma temperatures span 2.3−13 keV (with large uncertainties) and are broadly comparable to the hottest *XMM-Newton* component (5.2 ± 0.1 keV). As an additional test, we fitted all four eROSITA spectra simultaneously with a single absorbed plasma model, obtaining $kT = 6.5^{+1.1}_{-0.8}$ keV, slightly higher than the hottest *XMM-Newton* temperature but of the same order. The unabsorbed 0.2−12 keV fluxes derived for each epoch imply luminosities in the range $0.59 - 5.1 \times 10^{32}$ erg s^{-1} (assuming a distance of 496 pc; see Table 4), consistent with the long-term variability observed in the eROSITA light curve (top panel of Fig. 2).

3.4. System parameters

To obtain additional constraints on SRGt 062340's system parameters, we modelled its observed broadband spectral energy distribution (SED) from near-UV to infrared (IR) wavelengths. We compiled the SED using archival photometry along with our OM observation. Specifically, we retrieved optical *v*, *g*, *r*, *i*, and *z*-band data from the SkyMapper Southern Survey catalogue (Wolf et al. 2018),[5] and *B*, *V*, as well as Sloan *g*, *r*, and *i*-band magnitudes from the AAVSO Photometric All Sky Survey (APASS, Henden et al. 2015).[6] Additional optical data were taken from *Gaia* DR3 *G*, *BP*, and *RP* bands (Gaia Collaboration et al. 2016, 2023)[7] and the TESS mean magnitude *Tr* (Paegert et al. 2021).[8] Near-IR *J*, *H*, and *K* data were obtained from the Two Micron All Sky Survey (2MASS, Cutri et al. 2003; Skrutskie et al. 2006),[9] and IR *W*1, *W*2, and *W*3 magnitudes from the All-Sky Wide-field Infrared Survey Explorer (AllWISE, Wright et al. 2010).[10] For the UV regime, we used the mean UVM2-band flux/magnitude from our OM observation and archival UVW2-band data from *Swift* Ultra-Violet/Optical Telescope (*Swift*/UVOT, Roming et al. 2005). We note that SRGt 062340 was not included in the *Swift*/UVOT point-source catalogue (Yershov 2014; Page et al. 2014),[11] likely due to its high brightness causing saturation and pipeline failure.

[4] While EWs are conventionally negative for emission lines, we report the absolute value for clarity.

[5] https://cdsarc.cds.unistra.fr/viz-bin/cat/II/358
[6] https://cdsarc.cds.unistra.fr/viz-bin/cat/II/336
[7] https://cdsarc.cds.unistra.fr/viz-bin/cat/I/355
[8] https://cdsarc.cds.unistra.fr/viz-bin/cat/IV/39
[9] https://cdsarc.cds.unistra.fr/viz-bin/cat/II/246
[10] https://cdsarc.cds.unistra.fr/viz-bin/cat/II/328
[11] https://cdsarc.cds.unistra.fr/viz-bin/cat/II/339

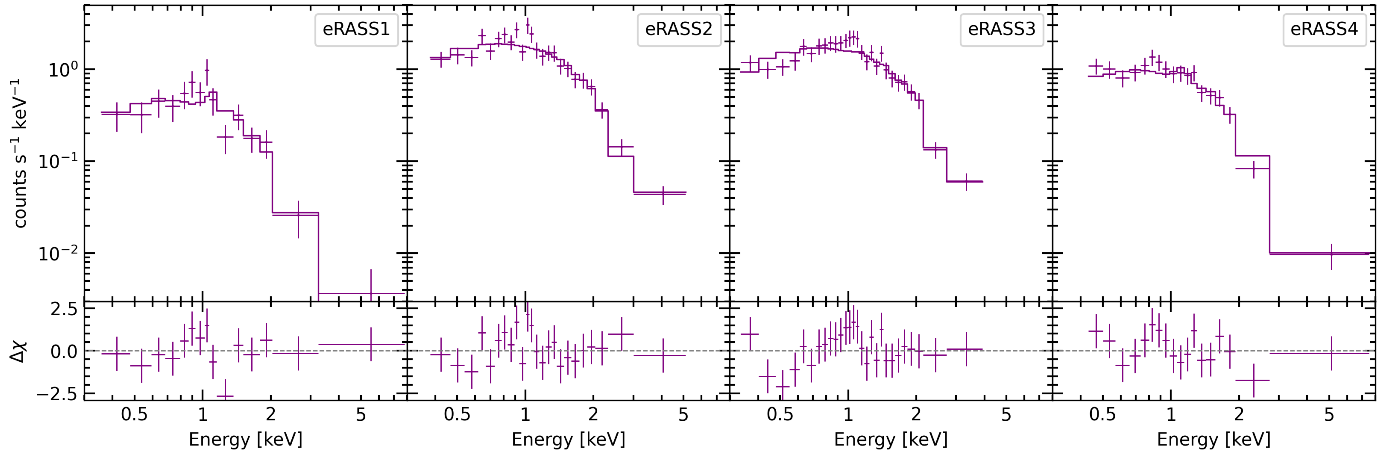

Fig. 5. eROSITA energy spectra of SRGt 062340 from the four observing epochs, shown with the best-fitting model (`TBabs*apec`). For clarity, we show the eRASS1 spectrum rebinned to 10 counts per bin, although the analysis was performed using a 1 count per bin spectrum (see text). For eRASS2-4, we show the 25 counts per bin spectra used in the analysis. Normalised residuals are shown in the bottom panels. The best-fitting parameters are listed in Table 4.

Table 5. System parameters adopted and derived for SRGt 062340 from SED modelling.

Adopted for the fit			
Parameter		Value	Reference
Inner radius of the disc	$R_{\rm in}$ [$R_\odot$]	0.0134	(1)
Outer radius of the disc	$R_{\rm out}$ [$R_\odot$]	0.531	(2)
Mass of the white dwarf	$M_{\rm WD}$ [$M_\odot$]	0.83	(3)
Radius of the white dwarf	$R_{\rm WD}$ [$R_\odot$]	0.0122	(4)
Surface gravity of the white dwarf	$\log(g_{\rm WD})$	8.19	(5)
Temperature of the boundary layer	$T_{\rm BL}$ [K]	10^5	(6)
Width of the boundary layer	$\Delta R_{\rm BL}$ [$R_\odot$]	0.00122	(7)
Mass of the donor	M_2 [$M_\odot$]	0.25	(8)
Radius of the donor	R_2 [$R_\odot$]	0.34	(8)
Temperature of the donor	T_2 [K]	3375	(8)
Surface gravity of the donor	$\log(g_2)$	4.78	(8)
Semi-major axis	A [$R_\odot$]	1.22	(9)
Derived from the fit			
Parameter		Value	Reference
Mass accretion rate	$\dot{M}$ [10^{-9} M$_\odot$ yr^{-1}]	6.8 ± 0.7	(10)
Inclination	i [°]	56 ± 2	(10)
Temperature of the white dwarf	$T_{\rm WD}$ [K]	~46000	(10)

References. (1) Frank et al. (2002, 1.1×R_{WD}); (2) Papaloizou & Pringle (1977, 0.9×R_{L1}); (3) Zorotovic et al. (2011); (4) Bédard et al. (2020); (5) Based on M_{WD} and R_{WD}; (6) Nabizadeh & Balman (2020); (7) 0.1×R_{WD}, between R_{WD} and R_{in}; (8) Knigge et al. (2011, $P_{\rm orb}$ = 3.6 h); (9) Based on M_{WD}, M_2, and $P_{\rm orb}$; (10) This work.

Nevertheless, given the importance of UV data to better constrain the mass accretion rate ($\dot{M}$), we manually extracted the UVW2 data and treat them as lower limits.

We modelled the observed SED of SRGt 062340 as the sum of four system components: the accretion disc, the white dwarf, a potential boundary layer, and the donor star. A detailed description of the modelling procedure and implementation of these components is provided in Appendix B. All parameter values adopted in the SED modelling are listed in Table 5. From the fit, we obtained $\dot{M}$ and the system inclination (i), which were treated as free parameters. Using the derived $\dot{M}$ and the relation in Eq. B.3, we inferred the white dwarf temperature ($T_{\rm WD}$). The best-fitting values, along with their 1σ uncertainties, are given in the lower section of Table 5.

The left panel of Fig. 6 shows the resulting SED along with the best-fitting model and its individual components. The observed SED exhibits a steep blue continuum, similar to that seen in the optical spectra (Schwope et al. 2022a), consistent with a dominant contribution from the accretion disc. Beyond approximately 10^4 Å, however, an IR excess becomes apparent, as observed in other nova-like CVs (Dhillon et al. 2000; Hoard et al. 2014). This IR upturn has been attributed to circumbinary dust (Hoard et al. 2009) or free-free emission from disc winds (Dubus et al. 2003). Additionally, there is a subtle trend for higher-inclination nova-like CVs to exhibit redder IR colours (Hoard et al. 2002, 2014), possibly due to the increasingly edge-on view of the cooler outer disc and rim at larger inclinations. Overall, the SED fitting provides a robust estimate of $\dot{M}$ and i for SRGt 062340 in its quasi-steady accretion state. However, we note a significant degeneracy between i and $\dot{M}$, evident from the diagonal trend in the 2D covariance plot shown in the right panel of Fig. 6.

4. Discussion

Although previous multi-wavelength studies left the subclassification of the CV SRGt 062340 uncertain (proposing it could be either an X-ray underluminous IP or an overluminous, non-magnetic nova-like, Schwope et al. 2022a), this study aims to clarify its nature by exploring both hypotheses. We analysed the source's variability on short (minutes to hours) and long (months to years) timescales using optical, UV, and X-ray light curves, and investigated its X-ray spectral properties based on a dedicated 46 ks *XMM-Newton* observation, complemented by the full eROSITA dataset and archival ASAS-SN optical photometry. In addition, we modelled the broadband SED, from near-UV to IR, to better constrain the system parameters.

4.1. X-ray and UV periodicities

SRGt 062340 displays significant variability on short timescales, as evidenced by the *XMM-Newton* light curves in Fig. 2 (panels 2-5), as well as on long timescales, as can be seen in the eROSITA light curve in the top panel of Fig. 2. The Lomb-Scargle power spectra of both the EPIC-pn and OM 30 s binned

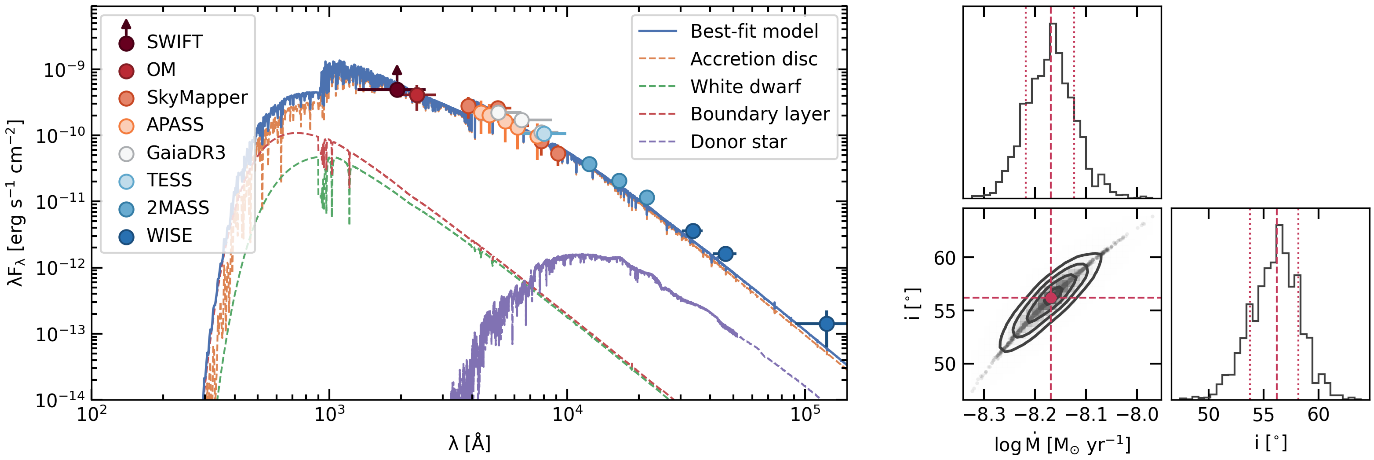

Fig. 6. *Left panel:* SED of SRGt 062340 as a function of wavelength, shown with the best-fitting model including contributions from the accretion disc, white dwarf, boundary layer, and donor star. *Right panel:* Corner plot of the posterior distributions from the SED fit, showing the joint and marginal probability densities for the mass-accretion rate ($\dot{M}$) and system inclination (i). The diagonal panels display the 1D marginalised Bayesian posteriors; the red dashed lines mark the median values and the red dotted lines indicate the 68% (1σ for a Gaussian distribution) credible intervals. The off-diagonal panel shows the 2D joint contours at the nominal 68%, 95%, and 99.7% (1σ, 2σ, and 3σ for a Gaussian distribution) credible intervals, illustrating the covariance between $\log(\dot{M})$ and i.

light curves revealed several modulations with a significance $>5\sigma$ (see Fig. 3 and Table 2). In particular, a modulation at 3.6 ± 0.5 h is evident in both datasets, with a significance $>8\sigma$. This value is typical of the orbital periods of nova-like and IP CVs (e.g. Inight et al. 2023), and it is fully consistent with a strong modulation (3.645 ± 0.006 h) found from optical spectroscopy by Brink et al. (in prep.). We therefore tentatively identify the 3.6 h modulation as the orbital period of SRGt 062340 and the 2 h and 1.4 h modulations as its harmonics (see Section 3.2).

Given its large error, our tentative orbital period is also consistent with the 3.94 ± 0.01 h modulation found in the first TESS dataset (Pichardo-Marcano 2020; Schwope et al. 2022a), which was subsequently confirmed by a 400-day interval ASAS-SN dataset (3.914 ± 0.001 h, Schwope et al. 2022a). However, this 3.9 h modulation is inconsistent with the 3.645 h value reported by Brink et al. (in prep.), and it was absent in the second TESS dataset obtained two years later. Contrary to the initial association with $P_{\rm orb}$ proposed by Pichardo-Marcano (2020), Brink et al. (in prep.) interpret the TESS modulation as a likely positive superhump period, produced by periodic tidal stresses from the secondary acting on the disc, which becomes eccentric and subsequently precesses (Whitehurst 1988; Lubow 1991).

As X-rays and UV emissions in CVs are expected to originate close to the white dwarf (either from its surface, an accretion column, or a boundary layer, Patterson & Raymond 1985; Mukai 2017), these spectral bands are well suited to detecting potential modulations at the white dwarf's spin period. Considering the possibility of a magnetic white dwarf in SRGt 062340, our timing analysis in Section 3.2, along with tentative correlations among several detected modulations, suggests two candidate spin periods: 36.0 ± 0.7 min and 43 ± 1 min. Both periods present meaningful correlations (see Table 3), including possible $P_{\rm beat}$ ($(\omega - \Omega)^{-1}$ or $(\omega + \Omega)^{-1}$) and harmonics, with the other significant peaks found in the EPIC-pn and OM power spectra. However, none of these modulations were detected in the optical data of SRGt 062340 (Brink et al. in prep.).

If SRGt 062340 were indeed an IP, the discrepancy between the modulations observed at different wavelengths would not be entirely unexpected, given the known variability in $P_{\rm spin}$ detection at different wavelengths in IPs. For example, in V1223 Sgr, $P_{\rm spin}$ is prominent in X-rays, while the dominant modulation in the optical is $P_{\rm beat}$ (see Jablonski & Steiner 1987, and references therein). Furthermore, the optical power spectra of FO Aqr, an IP exhibiting high and low optical states, presented by Littlefield et al. (2020, see their fig. 13), revealed that $P_{\rm spin}$ dominates the high states while $P_{\rm beat}$ and its harmonics dominate the low states. Additionally, the optical, UV, and X-ray emissions from CVs are expected to originate from different regions within the system. While the disc does not reach temperatures high enough to emit X-rays, it is a source of IR, optical an UV radiation (Mukai 2017). In contrast, the regions near the white dwarf, as previously discussed, are mostly responsible for producing X-rays, but also UV emissions. In the case of SRGt 062340, we observe similar variability in both UV and X-rays. However, the UV light curve shows stronger modulation at the potential $P_{\rm orb}$, while the X-rays are more significantly modulated at the tentative $P_{\rm spin}$. This suggests that the emissions in these bands may originate from slightly different regions in the system.

Although the origin of each modulation detected in SRGt 062340 is not yet fully understood, our results are somewhat comparable with previous findings. In addition to the 3.9 h TESS modulation, Schwope et al. (2022a) reported a 2080 ± 100 s (35 ± 2 min) modulation from SAAO high-speed photometry, as well as a $\sim$25 min modulation from the second TESS observation. The former is fully consistent with our 36 min EPIC-pn modulation. The latter, while not directly comparable to any of the periodicities identified in this work, agrees with a 24.9 min modulation found by Brink et al. (in prep.) from new SAAO photometry.

The presence of short-timescale, aperiodic variability (flickering) in the EPIC-pn light curve (Fig. 2), previously analysed in Section 3.2, points to intrinsic variability in the source's emission rather than being caused by absorption effects. While the exact origin remains uncertain, such flickering may result from varying shocks in a potential boundary layer or from rapid fluctuations in the accretion flow onto the white dwarf, possibly occurring along an extended accretion arc.

4.2. On the nature of the CV

The ASAS-SN long-term optical light curve (see Fig. 1) reveals two distinct drops in brightness: one of ∼3 mag, followed by another of ∼1 mag. These declines are characteristic of VY Scl-type nova-likes and firmly establish SRGt 062340 as a nova-like CV. However, while nova-likes are typically considered non-magnetic, the timing properties discussed in the previous section suggest the possible presence of a magnetic white dwarf in this system.

From our spectral analysis of SRGt 062340 (see Section 3.3) we find that the best-fitting model to the *XMM-Newton* spectra reveals a multi-temperature plasma, with components at $kT_1 = 0.23$ keV, $kT_2 = 0.94$ keV, and $kT_3 = 5.2$ keV. These temperatures likely correspond to emission from regions close to the white dwarf, such as a post-shock region, boundary layer, corona, or a combination of these. The plasma temperatures derived from the eROSITA spectra (kT = 2.3, 13, 9, and 4.8 keV) differ from the *XMM-Newton* results but are broadly comparable once their large uncertainties are taken into account (see Table 4). Non-magnetic CVs of the dwarf novae type typically exhibit plasma temperatures below 10 keV (Byckling et al. 2010), while IPs tend to show higher values in the ≃10−50 keV range (e.g. Barlow et al. 2006; Landi et al. 2009; Brunschweiger et al. 2009). The inferred temperatures in SRGt 062340 are therefore somewhat low for a typical IP and more consistent with non-magnetic CVs. However, we note that neither *XMM-Newton* nor eROSITA is particularly sensitive to high-energy emission, although both remain useful for constraining high-temperature plasma components (e.g. Worpel et al. 2020). For comparison, an *XMM-Newton* analysis of the nova-like MV Lyr revealed plasma temperatures of kT_1∼1 keV and kT_2∼6 keV (Dobrotka et al. 2017), consistent with our findings and supportive of a nova-like classification for SRGt 062340. Furthermore, our best-fitting model did not require a partial-covering absorber (commonly used in IP spectral models to account for X-ray emission from the accretion column, Norton & Watson 1989; Mukai 2017), which also favours a non-magnetic interpretation. Nonetheless, low plasma temperatures have been observed in the prototypical IP: DQ Her. In that case, an *XMM-Newton* analysis yielded $kT_1 = 0.27$ keV and $kT_2 = 0.84$ keV, interpreted as evidence of extensive reprocessing (Worpel et al. 2020), although a partial-covering absorber was required. Similarly, the IP nature of XMMU J185330.7-012815 was confirmed based on *XMM-Newton* data, modelled with a multi-temperature plasma ($kT_1 = 0.65$ keV, $kT_2 = 1.78$ keV, $kT_3 = 10.84$ keV), no partial-covering absorber, and a hydrogen column density of $\sim 5 \times 10^{20}$ cm^{-2} (Hui et al. 2012), a spectral configuration similar to that of SRGt 062340. These cases suggest that, despite the relatively low plasma temperatures, our spectral analysis does not rule out a magnetic nature. Finally, while polars generally exhibit lower plasma temperatures than IPs (e.g Schwope et al. 2007, 2020b), the presence of an accretion disc in SRGt 062340—evidenced by its optical light curve (Fig. 1), SED (Section 3.4 and Fig. 6), and the frequency break identified in the optical periodogram (Brink et al. in prep.)—effectively rules out a polar classification.

Table 4 lists the unabsorbed bolometric (0.01−100 keV) luminosities for all epochs. Our values, $0.63 - 5.3 \times 10^{32}$ erg s^{-1}, are of the same order as the 4.8×10^{32} erg s^{-1} bolometric luminosity reported by Schwope et al. (2022a) for eRASS2; for that epoch we obtain $(5.3 \pm 0.2) \times 10^{32}$ erg s^{-1}. The unabsorbed 0.25−10 keV X-ray luminosities of SRGt 062340 ($\gtrsim 10^{32}$ erg s^{-1}; Table 4) place it between the most luminous non-magnetic CVs, whose luminosities in this band typically span $10^{30} - 10^{32}$ erg s^{-1} (Wada et al. 2017, see also Byckling et al. 2010; Inight et al. 2022), and IPs, which generally exhibit higher X-ray luminosities (de Martino et al. 2020; Schwope et al. 2024). Moreover, we note the existence of low-luminosity IPs, identified by their optical brightness, which is strongly correlated with their low X-ray luminosities ($L_X < 10^{32}$ erg s^{-1}, Mukai & Pretorius 2023). Interestingly, a few members of the emerging population of magnetic nova-likes (discussed below) fall into this low-luminosity IP category.

The Fe Kα complex, including the fluorescent line at 6.4 keV produced by reflection, is observed across all types of CVs. Although a broad range of EW values has been reported in the literature, the average EW of the fluorescent line in dwarf novae is ∼60 eV, while in IPs it is ∼115 eV (see Xu et al. 2016, and references therein). The EW derived for SRGt 062340 in Section 3.3 (150^{+60}_{-50} eV) is consistent with the values typically observed in IPs. However, the amount of reflection depends on several factors intrinsic to the source, regardless of system type. These include the abundance of the reflector, the angle between the reflecting surface and the line of sight, the photon index of the spectrum of the X-ray emission source, and, to a lesser extent, the hydrogen column density (Done & Osborne 1997; Ezuka & Ishida 1999; Ishida et al. 2009). As a result, the EW alone provides limited diagnostic power regarding the nature of the system.

The broadband SED fitting of SRGt 062340 described in Section 3.4, revealed a disc-dominated system. We estimated a mass accretion rate of $\sim 7 \times 10^{-9}$ M$_\odot$ yr^{-1}, a value consistent with those typically observed in nova-likes systems (e.g. Hewitt et al. 2020), but also within the range reported for IPs (e.g. de Martino et al. 2020). In addition, we inferred a white dwarf temperature of $T_{\rm WD} \simeq 46000$ K from the estimated $\dot{M}$, which is in good agreement with values derived for other nova-likes such as DW UMa ($T_{\rm WD} \simeq 50000$ K, Araujo-Betancor et al. 2002), MV Lyr ($T_{\rm WD} \simeq 47000$ K, Hoard et al. 2004), and ASAS J0714+7004 ($T_{\rm WD} \simeq 41000$ K, Inight et al. 2022).

The link between nova-likes that exhibit low states and IPs has been explored in previous studies. Hameury & Lasota (2002, and references therein; see also Duffy et al. 2024) investigated the potential presence of magnetised white dwarfs in VY Scl-type nova-likes. The lack of dwarf-novae outburst cycles typically expected when the mass transfer rates decrease (leading to a drop in brightness) can be attributed to a magnetic field truncating the inner accretion disc. Such a magnetic field can be directly confirmed through the detection of pulsations on $P_{\rm spin}$ (e.g. Coughenour et al. 2022; Potter et al. 2024) and/or circular polarisation caused by cyclotron radiation (e.g. Lima et al. 2025), both indicative of the white dwarf's rotation. The observational evidence of spin modulations in white dwarfs within nova-likes is growing, as an increasing number of IPs exhibit the low states typical of VY Scl systems. These include DW Cnc (Rodriguez-Gil et al. 2004), V1323 Her (Andronov et al. 2014), FO Aqr (Littlefield et al. 2016), J183221.56-162724.25 (Beuermann et al. 2022), DO Dra (Hill et al. 2022), V515 And, V1223 Sgr, RX J2133+5107, V1025 Cen (Covington et al. 2022), SRGe J194401.8+284452 (Kolbin et al. 2024), AO Psc (Garnavich & Szkody 1988), Swift J2113.5+5422 (Halpern et al. 2018), V1062 Tau (Lipkin et al. 2004), and the IP candidate Swift J0746.3-1608 (Bernardini et al. 2019). Moreover, circular polarisation has been detected in some nova-like CVs of the SW Sex type (Rodriguez-Gil et al. 2001; Lima et al. 2021), a subclass defined by their distinctive optical spectroscopic features. Rodriguez-Gil et al. (2001) even proposed that SW Sex systems could be IPs with particularly high mass accretion rates.

In the case of SRGt 062340, we previously noted the presence of X-ray modulations that could tentatively be associated with $P_{\rm spin}$, although no corresponding signal is detected in the optical data. However, $P_{\rm spin}$ is often more clearly detected in X-rays than in optical wavelengths in IPs (see Section 4.1), and a lack of correlation between modulations at different wavelengths has already been observed in nova-likes, such as the SW Sex systems (Lima et al. 2021). The strong variability seen in the X-ray light curves of SRGt 062340 (on timescales ranging from minutes to years) is also a common characteristic of IPs (e.g. Norton et al. 1996). In addition to this general variability, we detected a < 20 days rebrightening during the optical low state (Fig. 1), which could correspond to a dwarf-nova-type outburst expected when the mass transfer rate decreases. This possibility does not contradict the magnetic white dwarf scenario proposed by Hameury & Lasota (2002), since their framework predicts an outburst cycle rather than only one or two isolated events. On the other hand, no circular polarisation has been detected in SRGt 062340 (see Brink et al. in prep. for details). Detecting polarisation can be particularly challenging in low-inclination systems, where the polarised emission from the region near the white dwarf may be diluted by the bright accretion disc (Lima et al. 2021). Although our SED fitting in Section 3.4 suggests an inclination of 56°, this value corresponds to the best fit and is strongly correlated with the mass accretion rate, leading to some degeneracy in the derived parameters (see Section 3.4). In fact, Brink et al. (in prep.) argue for a low inclination based on the small amplitude of the radial velocities of the Hβ and Hγ emission lines.

Despite the uncertainty surrounding the magnetic properties of SRGt 062340, the growing evidence for magnetic fields in nova-like CVs suggests that current classification schemes may need to be revisited and incorporated into broader models of CV evolution. Expanding the sample of confirmed magnetic nova-likes through dedicated polarimetric observations and high-sensitivity X-ray timing studies will be essential to quantifying the prevalence and role of magnetic fields in these systems.

5. Conclusions

We have investigated the nature of the CV SRGt 062340 using both dedicated *XMM-Newton* observations and eROSITA survey data, complemented by archival broadband photometry from the near-UV to the IR. The ASAS-SN long-term optical light curve, together with our broadband SED modelling, firmly establishes SRGt 062340 as a nova-like system. X-ray spectral analysis reveals emission from a multi-temperature plasma, while timing analysis suggests a tentative orbital period of 3.6 h. The power spectra show additional short-timescale (minutes to hours) variability which, combined with the pronounced long-term (months to years) X-ray variability seen in the eROSITA light curve and the X-ray luminosities of $\gtrsim 10^{32}$ erg s^{-1}, also makes SRGt 062340 a candidate IP. Under this hypothetical scenario, the detected modulations at 36 min and 43 min are both plausible candidates for the white dwarf's spin period. While the detection of such a spin modulation is often sufficient to confirm a magnetic nature, the uncertainty surrounding all observed modulations (across multiple datasets and wavelengths) combined with the nova-like classification, means that the magnetic nature of SRGt 062340 remains uncertain. A consistent detection of a spin-related modulation and/or circular polarisation would be required to confirm the IP scenario. Notably, while nova-likes are typically considered non-magnetic, a dual classification as both nova-like and IP is possible, as evidenced by the growing number of confirmed IPs that exhibit the typical low states of VY Scl nova-likes.

Acknowledgements. We thank the anonymous referee for their useful and thoughtful comments, which helped to improve this paper. VAC acknowledges support from the Deutsches Zentrum für Luft- und Raumfahrt (DLR) under contract 50 OR 2405, and JK from DLR under contract 50 OR 2408. JB is supported by the Deutsche Forschungsgemeinschaft (DFG, German Research Foundation) through grant Schw536/37-1. MV acknowledges support from the Science and Technology Facilities Council (STFC) studentship ST/W507428/1. This research has made use of data and/or software provided by the High Energy Astrophysics Science Archive Research Center (HEASARC), which is a service of the Astrophysics Science Division at NASA/GSFC. Based on observations obtained with XMM-Newton, an ESA science mission with instruments and contributions directly funded by ESA Member States and NASA. This work is based on data from eROSITA, the soft X-ray instrument aboard SRG, a joint Russian-German science mission supported by the Russian Space Agency (Roskosmos), in the interests of the Russian Academy of Sciences represented by its Space Research Institute (IKI), and the Deutsches Zentrum für Luft- und Raumfahrt (DLR). The SRG spacecraft was built by Lavochkin Association (NPOL) and its subcontractors, and is operated by NPOL with support from the Max Planck Institute for Extraterrestrial Physics (MPE). The development and construction of the eROSITA X-ray instrument was led by MPE, with contributions from the Dr. Karl Remeis Observatory Bamberg & ECAP (FAU Erlangen-Nuernberg), the University of Hamburg Observatory, the Leibniz Institute for Astrophysics Potsdam (AIP), and the Institute for Astronomy and Astrophysics of the University of Tübingen, with the support of DLR and the Max Planck Society. The Argelander Institute for Astronomy of the University of Bonn and the Ludwig Maximilians Universität Munich also participated in the science preparation for eROSITA. The eROSITA data shown here were processed using the eSASS software system developed by the German eROSITA consortium. This work incorporated data provided by ASAS-SN. ASAS-SN is funded by Gordon and Betty Moore Foundation grants GBMF5490 and GBMF10501 and the Alfred P. Sloan Foundation grant G-2021-14192. This work made use of `astropy` (http://www.astropy.org): a community-developed core Python package and an ecosystem of tools and resources for astronomy (Astropy Collaboration et al. 2013, 2018, 2022). We also made use of `numpy` (Harris et al. 2020), `scipy` (Virtanen et al. 2020), and `matplotlib` (Hunter 2007) PYTHON packages.

References

Allard, F., Homeier, D., & Freytag, B. 2012, Models of very-low-mass stars, brown dwarfs and exoplanets
Andronov, I. L., Dubovsky, P., Yoon, J.-N., & Kim, Y. 2014, ATEL, 5944, 1
Araujo-Betancor, S., Knigge, C., Long, K. S., et al. 2002, ApJ, 583, 437
Arnaud, K. A. 1996, in ASPC, Vol. 101, 17
Astropy Collaboration, Price-Whelan, A. M., Lim, P. L., et al. 2022, ApJ, 935, 167
Astropy Collaboration, Price-Whelan, A. M., Sipőcz, B. M., et al. 2018, AJ, 156, 123
Astropy Collaboration, Robitaille, T. P., Tollerud, E. J., et al. 2013, A&A, 558, A33
Ballouz, R.-L. & Sion, E. M. 2009, ApJ, 697, 1717
Baluev, R. V. 2008, MNRAS, 385, 1279
Barbary, K. 2021, extinction: Dust extinction laws, Astrophysics Source Code Library, [record ascl:2102.026]
Barlow, E. J., Knigge, C., Bird, A. J., et al. 2006, MNRAS, 372, 224
Bédard, A., Bergeron, P., Brassard, P., & Fontaine, G. 2020, ApJ, 901, 93
Belyakov, K. V., Suleimanov, V. F., Nikolaeva, E. A., & Borisov, N. V. 2010, in 17th European White Dwarf Workshop. AIP Conference Proceedings, ed. K. Werner & T. Rauch, Vol. 1273 (AIP), 342–345
Bernardini, F., de Martino, D., Mukai, K., & Falanga, M. 2019, MNRAS, 484, 101
Beuermann, K., Breitenstein, P., & Schwab, E. 2022, A&A, 657, A101
Brunner, H., Liu, T., Lamer, G., et al. 2022, A&A, 661, A1
Brunschweiger, J., Greiner, J., Ajello, M., & Osborne, J. 2009, A&A, 496, 121
Byckling, K., Mukai, K., Thorstensen, J. R., & Osborne, J. P. 2010, MNRAS, 408, 2298
Cannizzo, J. K. 1993, ApJ, 419, 318
Coleman, M. S., Rafikov, R. R., & Philippov, A. A. 2022, MNRAS, 512, 2945
Coppejans, R., Gulbis, A. A. S., Kotze, M. M., et al. 2013, PASP, 125, 976
Coughenour, B. M., Tomsick, J. A., Shaw, A. W., et al. 2022, MNRAS, 511, 4582
Covington, A. E., Shaw, A. W., Mukai, K., et al. 2022, ApJ, 928, 164
Cropper, M. 1990, Space Sci. Rev., 54, 195

Cutri, R. M., Skrutskie, M. F., van Dyk, S., et al. 2003, 2MASS All Sky Catalog of point sources
de Martino, D., Bernardini, F., Mukai, K., Falanga, M., & Masetti, N. 2020, Advances in Space Research, 66, 1209
den Herder, J. W., Brinkman, A. C., Kahn, S. M., et al. 2001, A&A, 365, L7
Dhillon, V. S., Littlefair, S. P., Howell, S. B., et al. 2000, MNRAS, 314, 826
Dobrotka, A., Ness, J. U., Mineshige, S., & Nucita, A. A. 2017, MNRAS, 468, 1183
Done, C. & Osborne, J. P. 1997, MNRAS, 288, 649
Doroshenko, V. 2024, arXiv, arXiv:2403.03127
Dubus, G., Campbell, R., Kern, B., Taam, R. E., & Spruit, H. C. 2003, MNRAS, 349, 869
Duffy, C., Wu, K., Ramsay, G., et al. 2024, MNRAS, 535, 3035
Eggleton, P. P. 1983, ApJ, 268, 368
Ezuka, H. & Ishida, M. 1999, ApJS, 120, 277
Fitzpatrick, E. 1999, PASP, 111, 63
Fouesneau, M. 2025, pyphot, https://doi.org/10.5281/zenodo.14712174
Frank, J., King, A., & Raine, D. J. 2002, Accretion Power in Astrophysics: Third Edition (Cambridge, UK: Cambridge University Press), 398
Gaia Collaboration, Prusti, T., De Bruijne, J. H., et al. 2016, A&A, 595, A1
Gaia Collaboration, Vallenari, A., Brown, A. G., et al. 2023, A&A, 674, A1
Garnavich, P. & Szkody, P. 1988, PASP, 100, 1522
Girish, V., Rana, V. R., & Singh, K. P. 2007, ApJ, 658, 525
Halpern, J. P., Thorstensen, J. R., Cho, P., et al. 2018, AJ, 155, 247
Hameury, J. M. 2020, Advances in Space Research, 66, 1004
Hameury, J. M. & Lasota, J. P. 2002, A&A, 394, 231
Harris, C. R., Millman, K. J., van der Walt, S. J., et al. 2020, Nature, 585, 357
Hart, K., Shappee, B. J., Hey, D., et al. 2023, arXiv, arXiv:2304.03791
Hellier, C. & Mukai, K. 2004, MNRAS, 352, 1037
Henden, A. A., Levine, S., Terrell, D., & Welch, D. L. 2015, American Astronomical Society, AAS Meeting #225, id.336.16, 225, 336.16
Hertfelder, M., Kley, W., Suleimanov, V., & Werner, K. 2013, A&A, 560, A56
Hewitt, D. M., Pretorius, M. L., Woudt, P. A., et al. 2020, MNRAS, 496, 2542
Hill, K. L., Littlefield, C., Garnavich, P., et al. 2022, AJ, 163, 246
Hoard, D. W., Kafka, S., Wachter, S., et al. 2009, ApJ, 693, 236
Hoard, D. W., Linnell, A. P., Szkody, P., et al. 2004, ApJ, 604, 346
Hoard, D. W., Long, K. S., Howell, S. B., et al. 2014, ApJ, 786, 68
Hoard, D. W., Wachter, S., Clark, L. L., & Bowers, T. P. 2002, ApJ, 565, 511
Hubeny, I. & Long, K. S. 2021, MNRAS, 503, 5534
Hui, C. Y., Sriram, K., & Choi, C. S. 2012, MNRAS, 419, 314
Hunter, J. D. 2007, Computing in Science & Engineering, 9, 90
Inight, K., Gänsicke, B. T., Blondel, D., et al. 2022, MNRAS, 510, 3605
Inight, K., Gänsicke, B. T., Breedt, E., et al. 2023, MNRAS, 524, 4867
Ishida, M., Okada, S., Hayashi, T., et al. 2009, PASP, 61, S77
Jablonski, F. & Steiner, J. E. 1987, ApJ, 323, 672
Jansen, F., Lumb, D., Altieri, B., et al. 2001, A&A, 365, L1
Jensen, K. A. 1984, ApJ, 278, 278
King, A. R. & Cannizzo, J. k. 1998, ApJ, 499, 348
Knigge, C., Baraffe, I., & Patterson, J. 2011, ApJS, 194, 28
Kolbin, A. I., Karpova, A. V., Suslikov, M. V., et al. 2024, Astronomy Letters, 50, 351
Kurpas, J., Schwope, A. D., Pires, A. M., & Haberl, F. 2024, A&A, 687, A251
Landi, R., Bassani, L., Dean, A. J., et al. 2009, MNRAS, 392, 630
Lasota, J. P. 2001, New Astronomy Reviews, 45, 449
Levenhagen, R. S., Diaz, M. P., Coelho, P. R. T., & Hubeny, I. 2017, ApJS, 231, 1
Lima, I. J., Rodrigues, C. V., Lopes, C. E. F., et al. 2021, AJ, 161, 225
Lima, I. J., Tovmassian, G., Rodrigues, C. V., et al. 2025, ApJ, 984, 152
Lipkin, Y. M., Leibowitz, E. M., & Orio, M. 2004, MNRAS, 349, 1323
Littlefield, C., Garnavich, P., Kennedy, M. R., et al. 2016, ApJ, 833, 93
Littlefield, C., Garnavich, P., Kennedy, M. R., et al. 2020, ApJ, 896, 116
Lomb, N. R. 1976, Ap&SS, 39, 447
Long, K. S., Mauche, C. W., Raymond, J. C., Szkody, P., & Mattei, J. A. 1996, ApJ, 469, 841
Lubow, S. H. 1991, ApJ, 381, 259
Lynden-Bell, D. 1969, Nature, 223, 690
Mason, K. O., Breeveld, A., Much, R., et al. 2001, A&A, 365, L36
Merloni, A., Lamer, G., Liu, T., et al. 2024, A&A, 682, A34
Morton, T. D. 2015, ASCL, ascl:1503.010
Mukai, K. 2017, PASP, 129, 062001
Mukai, K., Kinkhabwala, A., Peterson, J. R., Kahn, S. M., & Paerels, F. 2003, ApJ, 586, L77
Mukai, K. & Pretorius, M. L. 2023, MNRAS, 523, 3192
Nabizadeh, A. & Balman, Ş. 2020, Advances in Space Research, 66, 1139
Norton, A. J., Beardmore, A. P., & Taylor, P. 1996, MNRAS, 280, 937
Norton, A. J. & Watson, M. G. 1989, MNRAS, 237, 853
Ok, S., Lamer, G., Schwope, A., et al. 2023, A&A, 672, A188
Osaki, Y. 1996, PASP, 108, 39
Paczynski, B. 1977, ApJ, 216, 822
Paegert, M., Stassun, K. G., Collins, K. A., et al. 2021, eprint arXiv:2108.04778, arXiv:2108.04778
Page, M., Yershov, V., Breeveld, A., et al. 2014, in Proceedings of Science (Proceedings of Science (PoS)), 37
Papaloizou, J. & Pringle, J. E. 1977, MNRAS, 181, 441
Patterson, J. 1994, PASP, 106, 209
Patterson, J. & Raymond, J. C. 1985, ApJ, 292, 550
Pavlenko, E. P. & Shugarov, S. Y. 1999, A&A, 343, 909
Pavlinsky, M., Tkachenko, A., Levin, V., et al. 2021, A&A, 650, A42
Pichardo-Marcano, M. 2020, ATEL, 14222, 1
Popham, R. & Narayan, R. 1995, ApJ, 442, 337
Potter, S. B., Buckley, D. A., Scaringi, S., et al. 2024, MNRAS, 532, L21
Predehl, P., Andritschke, R., Arefiev, V., et al. 2021, A&A, 647, A1
Puebla, R. E., Diaz, M. P., & Hubeny, I. 2007, AJ, 134, 1923
Rana, V. R., Singh, K. P., Schlegel, E. M., & Barrett, P. E. 2006, ApJ, 642, 1042
Ricker, G. R., Winn, J. N., Vanderspek, R., et al. 2015, Journal of Astronomical Telescopes, Instruments, and Systems, 1, 014003
Rodriguez-Gil, P., Casares, J., Martinez-Pais, I. G., Hakala, P., & Steeghs, D. 2001, ApJ, 548, L49
Rodriguez-Gil, P., Gaensicke, B. T., Araujo-Betancor, S., & Casares, J. 2004, MNRAS, 349, 367
Roming, P. W. A., Kennedy, T. E., Mason, K. O., et al. 2005, Space Sci. Rev., 120, 95
Scargle, J. D. 1982, ApJ, 263, 835
Schachter, J., Filippenko, A. V., Kahn, S. M., & Paerels, F. B. S. 1991, ApJ, 373, 633
Schwope, A., Buckley, D. A., Kawka, A., et al. 2022a, A&A, 661, A42
Schwope, A., Buckley, D. A., Malyali, A., et al. 2022b, A&A, 661, A43
Schwope, A., Knauff, K., Kurpas, J., et al. 2024, A&A, 690, A243
Schwope, A., Semena, A., Maitra, C., et al. 2020a, ATel, 14219, 1
Schwope, A. D. 2025, A&A, 698, A106
Schwope, A. D., Staude, A., Koester, D., & Vogel, J. 2007, A&A, 469, 1027
Schwope, A. D., Worpel, H., Traulsen, I., & Sablowski, D. 2020b, A&A, 642, A134
Shakura, N. I. & Sunyaev, R. A. 1973, A&A, 24, 337
Shappee, B. J., Prieto, J. L., Grupe, D., et al. 2014, ApJ, 788, 48
Skilling, J. 2004, in American Institute of Physics Conference Series, Vol. 735, 24th International Workshop on Bayesian Inference and Maximum Entropy Methods in Science and Engineering, ed. R. Fischer, R. Preuss, & U. V. Toussaint (AIP), 395–405
Skilling, J. 2006, Bayesian Analysis, 1, 833
Skrutskie, M. F., Cutri, R. M., Stiening, R., et al. 2006, AJ, 131, 1163
Speagle, J. S. 2020, MNRAS, 493, 3132
Strüder, L., Briel, U., Dennerl, K., et al. 2001, A&A, 365, L18
Sunyaev, R. A., Arefiev, V., Babyshkin, V., et al. 2021, A&A, 656, A132
Townsley, D. M. & Gänsicke, B. T. 2009, ApJ, 693, 1007
Traulsen, I., Schwope, A. D., Lamer, G., et al. 2020, A&A, 641, A137
Turner, M. J., Abbey, A., Arnaud, M., et al. 2001, A&A, 365, L27
Vines, J. I. & Jenkins, J. S. 2022, MNRAS, 513, 2719
Virtanen, P., Gommers, R., Oliphant, T. E., et al. 2020, Nature Methods, 17, 261
Wada, Q., Tsujimoto, M., Ebisawa, K., & Hayashi, T. 2017, PASP, 69
Wade, R. A. 1988, ApJ, 335, 394
Warner, B. 2003, Cataclysmic Variable Stars (Cambridge: Cambridge University Press)
Whitehurst, R. 1988, MNRAS, 232, 35
Wilms, J., Allen, A., & McCray, R. 2000, ApJ, 542, 914
Wolf, C., Onken, C. A., Luvaul, L. C., et al. 2018, Publications of the Astronomical Society of Australia, 35, 29
Worpel, H., Schwope, A. D., Traulsen, I., Mukai, K., & Ok, S. 2020, A&A, 639, A17
Wright, E. L., Eisenhardt, P. R., Mainzer, A. K., et al. 2010, AJ, 140, 1868
Xu, X.-j., Wang, Q. D., & Li, X.-D. 2016, ApJ, 818, 136
Yershov, V. N. 2014, Ap&SS, 354, 97
Zorotovic, M., Schreiber, M. R., & Gänsicke, B. T. 2011, A&A, 536, A42

Appendix A: Phase-folded light curves

Fig. A.1 shows the *XMM-Newton*/EPIC-pn and OM light curves folded on the 3.6 h, 43 min, and 36 min modulations discussed in Section 3.2. The data were folded using 20 phase bins, with phase zero set arbitrarily at the start of the EPIC-pn dataset (MJD 60055.498855949016). The pulse fraction (PF), which quantifies the degree of modulation, was estimated as

$$PF = \frac{R_{max} - R_{min}}{R_{max} + R_{min}}, \tag{A.1}$$

where R_{max} and R_{min} are the maximum and minimum count rates in the folded light curve, respectively.

Appendix B: SED modelling

We modelled the broadband spectral energy distribution (SED) of SRGt 062340 (Section 3.4), accounting for four key components of the system:

- **Accretion disc.** In nova-like CVs, the accretion disc is the primary source of near-UV to IR emission and is expected to dominate the observed SED (Belyakov et al. 2010; Inight et al. 2022). We modelled the disc as a set of $N = 1000$ concentric annuli extending from the inner radius ($R_{\rm in}$) to the outer radius ($R_{\rm out}$). The local effective temperature ($T_{\rm eff}$) of each annulus was determined by the flux per unit surface area (Q) at a given radius (R) in the disc (Lynden-Bell 1969; Shakura & Sunyaev 1973, see equation 2.6 in the latter):

$$Q(R) = \frac{3GM_{\rm WD}\dot{M}}{8\pi R^3}\left(1 - \sqrt{\frac{R_{\rm in}}{R}}\right) = \sigma T_{\rm eff}(R)^4. \tag{B.1}$$

  Here $M_{\rm WD}$ and $\dot{M}$ are the white dwarf mass and the mass accretion rate, respectively. The inner radius was assumed to be $R_{\rm in} = 1.1\,R_{\rm WD}$ (Cannizzo 1993; Frank et al. 2002), where $R_{\rm WD}$ is the radius of the white dwarf. $R_{\rm out}$ was set to 90% of the white dwarf's Roche lobe radius ($R_{\rm L1}$), following Papaloizou & Pringle (1977) and Paczynski (1977). $R_{\rm L1}$ can be approximated in terms of the system's semi-major axis (A) as (Eggleton 1983, equation 2)

$$R_{\rm out} = 0.9 \times R_{\rm L1} = 0.9 \times \frac{0.49q^{2/3}}{0.6q^{2/3} + \ln(1+q^{1/3})} \times A\,, \tag{B.2}$$

  where $q = M_{\rm WD}/M_2$ is the white dwarf-to-donor star mass ratio.
  We interpolated the spectrum of each disc annulus using stellar atmosphere models from the BT-Settl grid (Allard et al. 2012)[12] at the corresponding $T_{\rm eff}(R)$ (Eq. B.1), assuming a constant surface gravity $\log(g) = 4.0$ and solar metallicity. In reality, the surface gravity in the disc varies with radius, following $\log(g) = \Omega_{\rm K}^2\, z$, where $\Omega_{\rm K}$ is the Keplerian angular velocity and z is the height from the disc mid-plane. This results in $\log(g)$ values ranging from ~6–6.5 in the inner regions down to ~3 at the outer edge. However, in the absence of synthetic spectra computed for such extreme $\log(g)$ conditions, we adopted a representative median value of $\log(g) = 4.0$. While the limitations of applying synthetic stellar spectra to model accretion disc emission are well known (Wade 1988; Hubeny & Long 2021), this approach nonetheless offers a more realistic alternative to the overly simplistic blackbody approximation.
- **White dwarf.** The white dwarf temperature ($T_{\rm WD}$) in CVs has been extensively studied by Townsley & Gänsicke (2009), who showed that ongoing accretion leads to significant heating of the white dwarf's surface. Their analysis demonstrated that $T_{\rm WD}$ typically ranges from ~10000 K to ~50000 K, depending primarily on the system's long-term average mass accretion rate $\langle\dot{M}\rangle$. They also provided a scaling relation quantifying this dependence as

$$T_{\rm WD} = 1.7 \times 10^4\ {\rm K}\left(\frac{\langle\dot{M}\rangle}{10^{-10}M_\odot\ {\rm yr}^{-1}}\right)^{1/4}\left(\frac{M_{\rm WD}}{0.9M_\odot}\right), \tag{B.3}$$

  with $\langle\dot{M}\rangle \approx \dot{M}$ since we are dealing with a nova-like CV.
  The white dwarf flux at the given temperature (Eq. B.3) was modelled using a grid of synthetic spectra for hot white dwarfs (Levenhagen et al. 2017)[13]. The corresponding surface gravity was calculated based on an assumed white dwarf mass $M_{\rm WD} = 0.83\,M_\odot$ (the average value suggested for CVs by Zorotovic et al. 2011) and a radius $R_{WD} = 0.0122\,R_\odot$, obtained from the mass-radius relations of Bédard et al. (2020).[14] We fixed $M_{\rm WD}$ in the SED modelling to avoid its strong degeneracy with the accretion rate $\dot{M}$ (Eq. B.1).
- **Boundary layer.** In CVs, a hot transition region known as the boundary layer is thought to exist where the accretion disc meets the surface of the white dwarf (e.g. Warner 2003). In this region, a substantial fraction of the gravitational potential energy is converted into heat as the Keplerian flow of the disc material slows abruptly to match the white dwarf's rotational velocity. Temperatures can reach 10^5 K in the optically thick part of the boundary layer, and $\sim 10^{7-8}$ K in the optically thin regions believed to emit X-rays (Jensen 1984; Popham & Narayan 1995; Nabizadeh & Balman 2020). However, the boundary layer's detailed properties, including its geometry, energy-release efficiency, temperature profile, and even its very existence, remain uncertain, in part due to the strong attenuation of extreme-UV emission by interstellar extinction (e.g. Long et al. 1996; Hertfelder et al. 2013; Coleman et al. 2022).
  Since the boundary layer's emission peaks in the far/extreme UV (optically thick material), its contribution to the observed SED is expected to be minimal. To represent this component, we modelled a hot ring located at $R \approx R_{WD}$, with a width of $\Delta R_{\rm BL} = 0.1 \times R_{\rm WD}$, positioned between the inner edge of the accretion disc and the white dwarf's surface. A temperature of $T_{\rm BL} = 10^5$ K was adopted, and the ring's emission was modelled using the same synthetic spectral grid used for hot white dwarfs (Levenhagen et al. 2017). The surface gravity was set to $\log(g) = 7$, the lowest available in the grid, and within the expected range ($\log(g) \approx 6-8$) for this region.
- **Donor star.** The physical parameters of the donor star (mass, radius, surface gravity, and effective temperature) were adopted from the evolutionary models for CVs presented by Knigge et al. (2011, see their table 2),[15] based on

[12] https://svo2.cab.inta-csic.es/theory/newov2/index.php?models=bt-settl-agss

[13] https://svo2.cab.inta-csic.es/theory/newov2/index.php?models=levenhagen17

[14] https://www.astro.umontreal.ca/~bergeron/CoolingModels/

[15] https://cdsarc.cds.unistra.fr/viz-bin/cat/J/ApJS/194/28

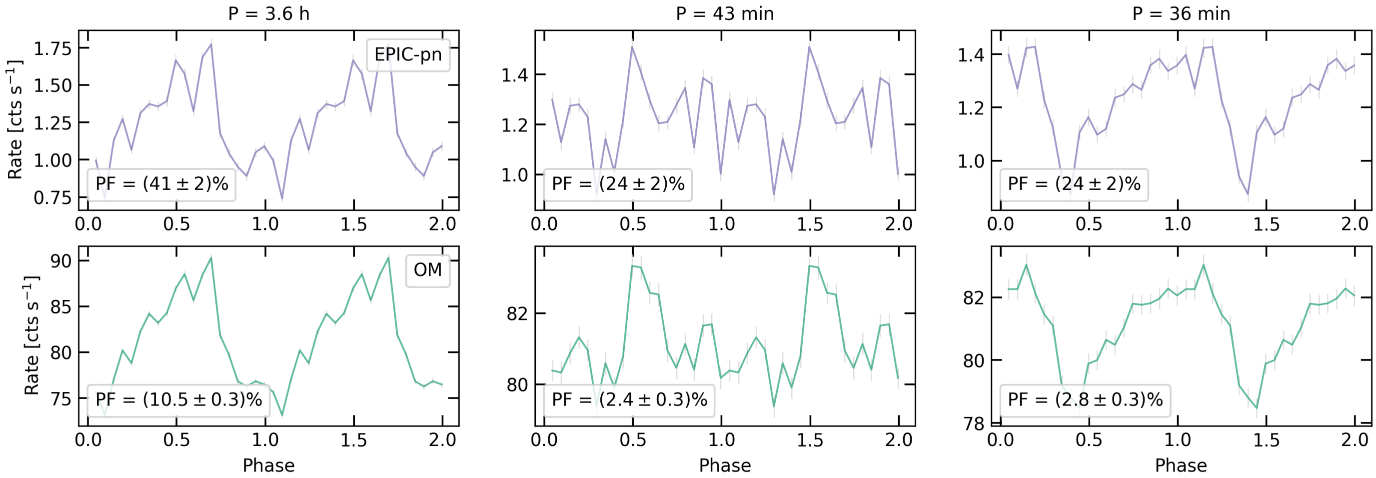

Fig. A.1. *XMM-Newton*/EPIC-pn (top panels) and OM (bottom panels) light curves folded on the 3.6 h, 43 min, and 36 min modulations. Two cycles are shown for clarity. In all cases, phase zero is defined arbitrarily at the start of the EPIC-pn dataset (MJD 60055.498855949016). PF denotes the pulse fraction.

the tentative orbital period of 3.6 h. Assuming solar metallicity, we interpolated the donor's spectrum from the same BT-Settl grid used for the accretion disc (Allard et al. 2012).

The interstellar absorption toward SRGt 062340 is relatively low, with $A_V \lesssim 0.05$ according to Doroshenko (2024),[16] consistent with our estimates of N_H (see Table 4). We applied extinction corrections using the `extinction Python` package (Barbary 2021),[17] adopting $A_V = 0.05$ and the extinction law from Fitzpatrick (1999).

We fitted the mass accretion rate ($\dot{M}$) and system inclination (i) by imposing a lower bound on the $\dot{M}$ prior to ensure the disc remains in a hot, stable state; specifically, requiring $T_{eff}(R_{out}) >= 6000$ K (current estimations lie within 6000 – 8000 K; see Lasota 2001, and references therein). A uniform prior was adopted for the inclination, ranging from 0° to 90°. The fit was performed within a Bayesian inference framework using the nested sampling algorithms (Skilling 2004, 2006), as implemented in the `dynesty Python` package (Speagle 2020).[18] This technique, although designed for computing Bayesian evidence, employs MCMC-style constrained sampling to explore the posterior, making it conceptually similar to conventional MCMC methods. To improve computational efficiency and avoid interpolation artefacts when using synthetic atmosphere models, we did not generate a full model spectrum for each point in parameter space. Instead, we precomputed a grid of synthetic photometric fluxes (e.g. V, B, J bands) for each spectral model using the `pyphot` tool (Fouesneau 2025).[19] During fitting, we interpolated the corresponding band fluxes from this precomputed grid using the `isochrones` interface (Morton 2015).[20] The resulting synthetic photometry was then directly compared to the observed photometry. To account for both intrinsic variability of SRGt 062340 across different epochs and potential underestimation of measurement uncertainties, we followed the approach of Vines & Jenkins (2022),[21] by introducing an additive excess noise term into the Gaussian log-likelihood for each band. This term was treated as a free parameter and allowed the photometric uncertainties to scale up to 10% of the measured flux values.

16 http://astro.uni-tuebingen.de/nh3d/nhtool
17 https://extinction.readthedocs.io/en/latest/
18 https://dynesty.readthedocs.io/en/v2.1.5/
19 https://mfouesneau.github.io/pyphot/index.html
20 https://github.com/timothydmorton/isochrones
21 https://github.com/jvines/astroARIADNE